THE TRANSIT TRANSMISSION SPECTRUM OF A COLD GAS GIANT PLANET

Paul A. Dalba[1], Philip S. Muirhead[1], Jonathan J. Fortney[2], Matthew M. Hedman[3],
Philip D. Nicholson[4], and Mark J. Veyette[1]

[1] Department of Astronomy, Boston University, 725 Commonwealth Avenue, Boston, MA 02215, USA; pdalba@bu.edu
[2] Department of Astronomy & Astrophysics, University of California, Santa Cruz, CA 95064, USA
[3] Department of Physics, University of Idaho, Moscow, ID 83843, USA
[4] Department of Astronomy, Cornell University, Ithaca, NY 14853, USA

ABSTRACT

We use solar occultations observed by the Visual and Infrared Mapping Spectrometer on board the *Cassini* Spacecraft to extract the 1–5 μm transmission spectrum of Saturn, as if it were a transiting exoplanet. We detect absorption from methane, ethane, acetylene, aliphatic hydrocarbons, and possibly carbon monoxide, with peak-to-peak features of up to 90 parts-per-million despite the presence of ammonia clouds. We also find that atmospheric refraction, as opposed to clouds or haze, determines the minimum altitude that could be probed during mid-transit. Self-consistent exoplanet atmosphere models show good agreement with Saturn's transmission spectrum but fail to reproduce a large absorption feature near 3.4 μm, likely caused by gaseous ethane and a C–H stretching mode of an unknown aliphatic hydrocarbon. This large feature is located in one of the *Spitzer Space Telescope* bandpasses and could alter interpretations of transmission spectra if not properly modeled. The large signal in Saturn's transmission spectrum suggests that transmission spectroscopy of cold, long-period gaseous exoplanets should be possible with current and future observatories. Motivated by these results, we briefly consider the feasibility of using a survey to search for and characterize cold exoplanets that are analogous to Jupiter and Saturn utilizing a target-of-opportunity approach.

Key words: planetary systems – planets and satellites: atmospheres – planets and satellites: individual (Saturn)

Supporting material: data behind figure

1. INTRODUCTION

To date, investigations of exoplanet atmospheres have not targeted atmospheres resembling the cold, gaseous planets in our solar system. Transit observations have only been used to characterize the atmospheres of exoplanets on short-period orbits (e.g., Charbonneau et al. 2002; Knutson et al. 2007; Pont et al. 2008; Fraine et al. 2014; Kreidberg et al. 2014a). Close-in exoplanets are warm, producing favorable atmospheric scale heights, and they transit their hosts frequently, providing many opportunities to characterize their atmospheres. Direct imaging observations, which require that exoplanets be self-luminous, have also only been able to characterize warm exoplanets; most directly imaged planets are younger than 50 Myr and hotter than 800 K (Marois et al. 2008; Lagrange et al. 2010; Carson et al. 2013). High-resolution, ground-based spectroscopy also favors short-period planets that experience large changes in radial-velocity during a single observation or have atmospheres that are warm enough to be observed in emission (e.g., Snellen et al. 2010; Birkby et al. 2013). Other observing techniques (i.e., radial-velocity and microlensing) effectively discover long-period, giant exoplanets but do not provide information pertaining to planets' atmospheres.

Transmission spectroscopy is the most appropriate known method for characterizing the atmospheres of cold, long-period planets resembling those in our solar system. Unfortunately, transit surveys are geometrically biased against long-period planets (Beatty & Gaudi 2008). According to the NASA Exoplanet Archive and the Exoplanet Orbit Database (Han et al. 2014),[5] of the 1230 confirmed exoplanets discovered via the transit method, only 5 (0.4%) have orbital semimajor axes

$a \gtrsim 1$ AU: Kepler-34b, Kepler-47c, Kepler-90h, Kepler-421b, and Kepler-452b (Orosz et al. 2012; Welsh et al. 2012; Cabrera et al. 2014; Kipping et al. 2014; Jenkins et al. 2015, respectively). Of these, only Kepler-421b has an equilibrium temperature below 200 K (assuming a Bond albedo of 0.3), making it nearly as cold as Jupiter. Having only this one member, the regime of transiting exoplanets that are analogous to the giant planets in our solar system has so far gone relatively unexplored.

Transmission spectra have the potential to reveal molecular abundances in exoplanet atmospheres, which constrain models of their thermal profiles (Fortney et al. 2010). Transmission spectra are also useful for full atmospheric retrieval codes (e.g., Irwin et al. 2008; Madhusudhan & Seager 2009; Line & Yung 2013; Line et al. 2014) that explore phenomena such as temperature inversions and disequilibrium chemistry, both of which have been observed in the solar system gas giants (Tokunaga et al. 1983; Bagenal et al. 2004; Baines et al. 2005; West et al. 2009).

Atmospheric abundances of molecules such as CO, CH_4, CO_2, and H_2O place constraints on C/O, C/H, and O/H ratios, which are tracers of planetary formation and evolution. Many planet formation theories, including that for Jupiter, invoke core accretion (Pollack et al. 1996; Owen et al. 1999), which has been tested by observations of C/O in hot Jupiters (e.g., Brogi et al. 2014; Line et al. 2014; Stevenson et al. 2014). Atmospheric abundance measurements of cold, giant exoplanets would provide a similar test of core accretion and could also be used to improve the current understanding of how atmospheric abundances respond to planetary migration (Ida & Lin 2004; Öberg et al. 2011; Madhusudhan et al. 2014).

---

[5] Both databases accessed on 2015 July 23.

Atmospheric abundances can be difficult or impossible to determine for atmospheres that harbor clouds or haze, which produce flat transmission spectra across near-infrared wavelengths (e.g., Bean et al. 2010; Berta et al. 2012; Ehrenreich et al. 2014; Knutson et al. 2014a, 2014b; Kreidberg et al. 2014a). Clouds are present in the atmospheres of each giant solar system planet (e.g., Lindal et al. 1987; Smith et al. 1989; Bagenal et al. 2004; West et al. 2009), but these planets are much colder and experience different levels of stellar insolation than previously observed cloudy exoplanets. It is not clear how these differences would influence the effects of clouds on the transmission spectrum of a cold giant exoplanet.

To begin exploring the regime of cold, long-period exoplanets, we turn to an extensively studied gas giant in our own solar system: Saturn. High-quality solar system observations provide a unique opportunity to study and "ground-truth" the methods used to characterize exoplanets. Solar system bodies such as the Earth (e.g., Pallé et al. 2009; Vidal-Madjar et al. 2010; García Muñoz et al. 2012; Bétrémieux & Kaltenegger 2013; Misra et al. 2014; Schwieterman et al. 2015), Titan (Robinson et al. 2014), Jupiter (Irwin et al. 2014; Montañés-Rodríguez et al. 2015), and Uranus and Neptune (Kane 2011) have all been studied in the context of extrasolar planetary science in recent years.

We use observations from the Visual and Infrared Mapping Spectrometer (Brown et al. 2004) on board the *Cassini* Spacecraft to extract the 1–5 μm transmission spectrum of Saturn, as if it were a transiting exoplanet. With this spectrum, we assess the feasibility of observing cold, gaseous exoplanets with current and future observatories.

We present the *Cassini*-VIMS observations, data, and analysis procedures in Section 2. In Section 3 we develop an occultation model that assumes that the portion of Saturn's atmosphere sampled by the observations is isothermal and in hydrostatic equilibrium. We also fit for the effects of atmospheric refraction and absorption versus ascribing them from previous observations. In Section 4, we calculate the transmission spectrum of Saturn and compare it to spectra of model atmospheres that are currently applied to exoplanets. Lastly, in Section 5 we discuss the implications of this work for exoplanet atmosphere models, and we briefly consider a strategy to locate and characterize cold, giant exoplanets in the near future.

2. OBSERVATIONS

2.1. Cassini-VIMS

The Visual and Infrared Mapping Spectrometer (VIMS) on board the *Cassini* Spacecraft has been observing Saturn and its satellites since arriving at the Saturnian system in 2004 (Matson et al. 2002; Brown et al. 2004). VIMS has two imaging grating spectrometers, VIMS-VIS and VIMS-IR, that operate in the visible (0.35–1.07 μm, 96 bands, $\sim$8 nm resolution) and near-IR (0.85–5.11 μm, 256 bands, $\sim$17 nm resolution), respectively. Only the latter is used during solar occultations. Solar occultation observations are obtained through a solar port with an aperture of 30 mm by 5 mm that is orientated 20° away from the boresight direction of the main aperture. In the solar port, sunlight undergoes several reflections that attenuate the solar flux by a factor of approximately 2.5 $\times$ 10^{-7} before passing through the slit and into the main optical path of VIMS-IR (Bellucci

et al. 2009). The nominal VIMS-IR observation produces a data cube comprised of two spatial dimensions (64 $\times$ 64 pixels) and one spectral dimension. The indium antimonide IR detector is a one-dimensional array (1 $\times$ 256 pixels), so it can only obtain the spectrum of a single spatial pixel at a time. Therefore, the IR telescope's secondary mirror is scanned in two dimensions across the target to construct a full data cube. For solar occultation observations, VIMS only acquires a 12 $\times$ 12 pixel field of view, which corresponds to an angular size of 20$\farcm$6 $\times$ 20$\farcm$6 (each pixel having an angular resolution of 1.7 arcminutes). This reduction in the field of view is acceptable since the solar disk as seen from Saturn only extends over approximately 2 $\times$ 2 pixels.

2.2. Occultation Data

We analyzed a Saturn-solar occultation observation from UT 2007 November 17. The observation consisted of 479 data cubes, each having an image dimension of 12 $\times$ 12 pixels and an exposure time of 20 ms per pixel. VIMS began observing several minutes before ingress in order to establish a high-signal measurement of the solar spectrum out of occultation. Similarly, the observation ended several minutes after the solar flux was completely attenuated. The duration of an entire observation was approximately 0.5 hr.

For each 12 $\times$ 12 pixel image, we determined a value of relative transmission (T_λ) by summing the signal over the entire field of view and dividing by the total signal of the Sun prior to occultation. Outside of occultation, $T_\lambda \sim 1$. Once the Sun's flux was completely attenuated by Saturn, $T_\lambda \sim 0$. We followed this normalization procedure for each of the 256 wavelength bands in each of the 479 data cubes. This ratio removed systematic and instrumental errors along with the the need to convert the detector's data numbers (or counts) into specific energies. Data calibration was further simplified by the high linearity of VIMS-IR detector (Brown et al. 2004) and by the low background signal compared to that of the Sun (less than 1%). The data we considered did not suffer from contamination by stray light entering the boresight, spacecraft pointing instability, or other sources of spurious signal that warrant advanced calibration procedures (e.g., Maltagliati et al. 2015). A formal data reduction routine for VIMS exists (McCord et al. 2004); however, it is not appropriate for observations of solar occultations that pass through a different optics chain than those acquired through the main aperture.

When calculating T_λ, we defined the background as all the pixels residing outside of a circular aperture centered on the Sun with a radius of four pixels. The average background was approximately 14 counts per pixel, only 0.6% of the average integrated signal from the Sun ($\sim$2260 counts). Since the background level decreased unevenly as Saturn's limb entered the field of view, we could not accurately estimate the background signal across the detector simply by finding the mean number of counts in a circular annulus surrounding the central aperture. Instead, we separated the detector into four 6 $\times$ 6-pixel quadrants, and subtracted the mean background locally in each. When Saturn's atmosphere was in view, the average background value was 1–2 counts per pixel. Considering the minimal contribution of the background to the total count value of the entire field of view, this simple procedure was sufficient.

After calculating T_λ, we median-filtered each occultation light curve to remove outliers due to other sources of spurious
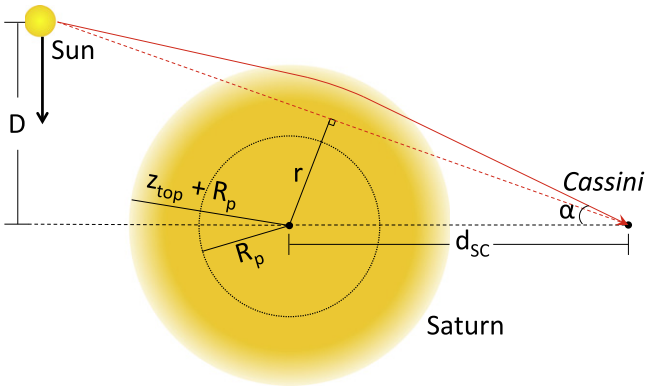
Figure 1. Geometry of the Sun–Saturn–*Cassini* system (not to scale, rings of Saturn not pictured). Light from the Sun followed a curved path in Saturn's atmosphere (solid red line). The tangent radius (r) was measured from the center of Saturn to the point along the straight line of sight between *Cassini* and the Sun (dashed red line) that was tangential to the local horizon of Saturn. In the model, rays from the Sun entered Saturn's atmosphere at an altitude of $R_p + z_{top}$ before reaching *Cassini* with angle α to the *Cassini*–Saturn line. R_p was the "surface" of Saturn from which the altitude z was measured. As the occultation progressed, the Sun appeared to move in the direction indicated by the black arrow from the point of view of *Cassini*. Each value of r corresponded to a value of D (Section 3.3). There was some impact parameter between the path of the Sun and the center of Saturn as seen from *Cassini* (i.e., the Sun did not pass directly behind the center of Saturn). However, the occultation model only tracked the one-dimensional radial motion of the Sun.

signal, most of which were cosmic ray strikes on the detector. A data point was declared an outlier and removed if it had a value of T_λ that was either 3σ above or below the median T_λ value of the six points on either side of it.

We assigned each T_λ-value an uncertainty that was equal to the standard deviation of solar signal prior to occultation. At redder wavelengths ($\lambda > 4\,\mu$m), the solar intensity was weak and the data became increasingly noisy. The eight reddest bands spanning 4.99–5.12 μm were used to record timing information for the observations and are not included in the following analysis. Some of the VIMS data exhibited low-level, time-correlated noise, possibly due to detector readout effects (McCord et al. 2004). The magnitude was typically on the order of the uncertainty and did not greatly affect the signal or the analysis.

We monitored the progress of the occultation with measurements of the "tangent radius" r. This was a measure of distance between the center of Saturn and the point on a straight line of sight between the Sun and *Cassini* that was tangential to the local horizon of Saturn (see Figure 1). We used r as a substitute for time since it included information about the relative positions of the Sun, Saturn, and *Cassini* that were useful when modeling the occultation.

3. A SOLAR OCCULTATION MODEL

3.1. Parameterizing Saturn's Atmosphere

A goal of this work was to measure Saturn's transmission spectrum as empirically as possible. Therefore, we modeled the Saturn-solar occultations without directly using atmospheric chemical abundances, mixing ratios, indices of refraction, and opacities available in the literature. Instead, we fit the VIMS occultation data to a model atmosphere and estimated parameters describing the structure and composition of Saturn's atmosphere. Each of *Cassini*-VIMS' wavelength bands had its own best-fit occultation light curve. For each wavelength band,

we assumed that the portion of Saturn's atmosphere sampled by the observation was ideal, isothermal, and in hydrostatic equilibrium in order to acquire the familiar number density profile

$$n(z) = n_0 e^{-z/H}, \qquad (1)$$

where z is altitude, $n(z)$ is particle number density as a function of altitude, and n_0 is the reference particle number density at the $z = 0$ m "surface" of Saturn (R_p), which approximately corresponded to the one-bar pressure level. H is the atmospheric scale height defined by

$$H = \frac{k_B \mathcal{T}}{\mu m_p g}, \qquad (2)$$

where k_B is Boltzmann's constant, $\mathcal{T}$ is temperature, μ is the mean molecular weight of Saturn's atmosphere, m_p is the proton mass, and g is the local acceleration due to gravity. H was a critical parameter to the occultation model, as it controlled how steeply the transmission decreased during ingress. The scale height did not have a wavelength-dependence *per se*, but we could not use a single value of H in the model across the spectrum. Due to methane absorption, different wavelengths sampled portions of Saturn's atmosphere that were separated by up to ∼450 km in altitude. This was readily observable in the occultation data as a range in "half-light" r-values, where $T_\lambda = 0.5$. Over ∼450 km, variations in temperature and therefore scale height necessitated that we fit for H at each wavelength in the model.

We used two parameters to describe the wavelength-dependent absorption and refraction of light in Saturn's atmosphere: the *total* absorption cross section σ_λ and the *total* refractivity ν_λ.[6] Both parameters included contributions from all atmospheric species. The other parameters in the model, R_p and n_0, were not wavelength-dependent so we adopted the following one-bar values for Saturn: $R_p = 5.7 \times 10^7$ m and $n_0 = 5.5 \times 10^{25}$ m^{-3} (Fouchet et al. 2009; Hubbard et al. 2009; West et al. 2009). This value of R_p accounted for Saturn's oblateness (∼0.0979) and the local Saturn-centric latitude of observation (∼49°S), assuming Saturn to be an oblate spheroid (e.g., Smith et al. 1983; Cox 2000).

In a vertically stratified atmosphere, refractivity $\nu(z)$ can be defined as

$$\nu(z) = \left[\frac{n(z)}{L_0} \right] \sum_j f_j(z) \nu_{0,j}, \qquad (3)$$

where L_0 is Loschmidt's Number, $f_j(z)$ is the altitude-dependent mole fraction of the jth atmospheric species, and $\nu_{0,\,j}$ is the refractivity of the jth species at standard temperature and pressure. Loschmidt's Number is merely a particle number density at some standard temperature and pressure, both of which are functions of altitude in Saturn's atmosphere. We set $L_0 = n_0$, the reference particle number density, such that $n(z)/L_0 = e^{-z/H}$. We also assumed that Saturn's atmosphere was well-mixed such that f_j did not have a z-dependence. This allowed us to treat the summation term in Equation (3) as a

---

[6] The refractivity (ν) is related to the index of refraction (η) by $\nu = \eta - 1$.

parameter and rewrite the entire equation as

$$\nu(z) = \nu_\lambda e^{-z/H}, \qquad (4)$$

where ν_λ is the wavelength-dependent total refractivity parameter described above.

We note that ν_λ was evaluated at $z = 0$ m, allowing for $\nu(z)$ to be calculated elsewhere in the atmosphere with Equation (4). For σ_λ, we assumed a well-mixed composition at the altitudes sampled by the observation at a given wavelength so that σ_λ did not have a z-dependence.

3.2. Ray Tracing

We traced rays between the Sun and *Cassini* according to a ray tracing scheme developed by Kivalov (2007).[7] Each ray had finite energy and could be bent by refraction and attenuated by absorption. The density of rays in a given area and solid angle represented the specific intensity from the Sun.

At the time of observation, we determined the orbital distance of Saturn ($a = 9.524$ AU) and the distance between *Cassini* and the center of Saturn ($d_{SC} = 2.59 \times 10^8$ m) using the JPL-HORIZONS solar system ephemeris computation service (Giorgini et al. 1996). We assumed that these distances were constant during the 0.5-hr observation period.

We considered rays that reached the spacecraft at a positive angle of α relative to the *Cassini*–Saturn line that ranged from zero to $\arcsin[(R_p + z_{top})/d_{SC}]$, where z_{top} was the fiducial "top" of Saturn's atmosphere equal to 1.2×10^6 m or ~ 20 scale heights (see Figure 1). At this altitude, the particle number density was reduced by a factor of 2×10^{-9} from n_0 and the atmosphere was essentially transparent.

The ray tracing scheme accounted for refraction by modeling each step of a ray's motion through Saturn's atmosphere as a circle segment where the radius of curvature was a function of the index of refraction (Kivalov 2007; van der Werf 2008). At each step, we calculated the optical depth (τ_λ) experienced by the ray according to

$$\frac{d\tau_\lambda}{ds} = n(z)\sigma_\lambda, \qquad (5)$$

where s is the ray path length. The rays propagated through Saturn's atmosphere until one of two conditions was met: 1) $z = z_{top}$, meaning that the ray reached the edge of the atmosphere on the *Cassini*-side, or 2) $\tau_\lambda = 50$, in which case the ray's energy had been fully attenuated.

3.3. Generating a Transmission Model

We made the occultation model in a reference frame such that Saturn and *Cassini* were fixed relative to each other and the Sun appeared to move[8] in a plane perpendicular to the *Cassini*–Saturn line (see the black arrow in Figure 1). This plane will herein be referred to as *the plane of the Sun*. Positions on this plane with respect to the *Cassini*–Saturn line were expressed with the coordinate D. Although D did not have a physical meaning, it allowed for direct comparison between the position of the Sun (from the data) and the rays' points of origin (from the model). The D-values of the Sun were calculated by
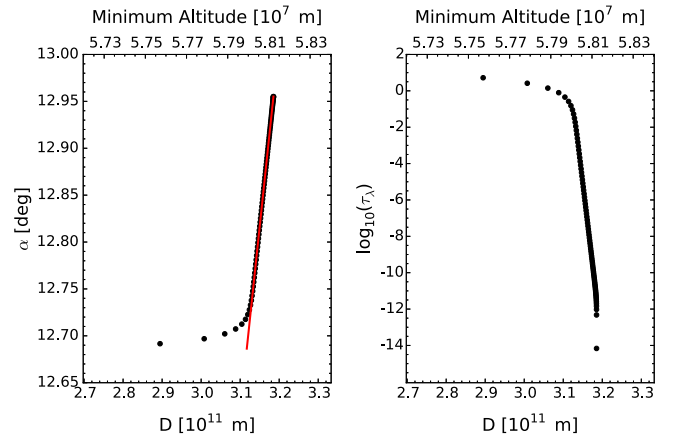
---

[7] A concise summary of this ray tracing scheme was provided by van der Werf (2008).
[8] This choice increased the computational efficiency of the model-fitting process.

Figure 2. Numerical relations between α, τ_λ, D, and the minimum altitude at 1.25-μm in the occultation model. Each ray (black data point) originated at the Sun with a D-value that corresponded to a value of α and τ_λ, which governed brightness losses by refraction and absorption, respectively. The minimum altitude in Saturn's atmosphere ($R_p + z$) achieved by each ray is also shown. These smooth functions allowed for interpolation of any D-value. The red line in the left panel shows the relation $\tan\alpha = D/(a + d_{SC})$, where D and $(a + d_{SC})$ are the opposite and adjacent sides of a right triangle, respectively, from Figure 1. Rays that only traverse Saturn's upper atmosphere (large α) lie along this red line because they do not experience high indices of refraction and therefore travel in nearly straight lines. However, rays deviate from the red line at lower α as refractive bending becomes more significant.

projecting r, the tangent radius, back to the plane of the Sun using the geometry of the system.

Each ray considered by the model could be described by three quantities: τ_λ, the final optical depth the ray achieved upon exiting Saturn's atmosphere; α, the angle above the *Cassini*–Saturn line at which the ray reached *Cassini*; and D, the height on the plane of the Sun above the *Cassini*–Saturn line where the ray originated. Both τ_λ and α were important for determining the decrease in brightness during the occultation. Figure 2 shows that these quantities had smooth, numerical relations that were amenable to interpolation. For any D-values occupied by the Sun during the occultation, we could numerically determine the τ_λ and α values of the Sun's rays. We also measured the minimum radial distance from the center of Saturn achieved by each ray. This distance was important for assessing the effects of refraction in the data (Section 3.5) and was physically more informative than D.

The τ_λ-values allowed us to determine the energy attenuation due to absorption. The α-values allowed us to determine flux losses due to refraction. Atmospheric refraction caused an apparent shrinking of the solar disk in the vertical (or radial) direction (see Figure 3). This change in shape resulted from the differential refraction experienced by rays originating at different points on the Sun. A ray leaving the "top" of the Sun traveled through a less dense portion of the atmosphere than a ray leaving from the "bottom" of the Sun. Consequently, the difference in α for these two rays and therefore the apparent angular size of the Sun on the detector diminished as the occultation progressed—resulting in a loss of brightness. Another result of atmospheric refraction was the separation of the *apparent* position of the Sun and the *true* position of the Sun. Since *Cassini* pointed toward the true position of the Sun throughout the occultation observation, this phenomenon manifested itself as an apparent motion of the Sun on the detector. Figure 3 illustrates that the occultation model
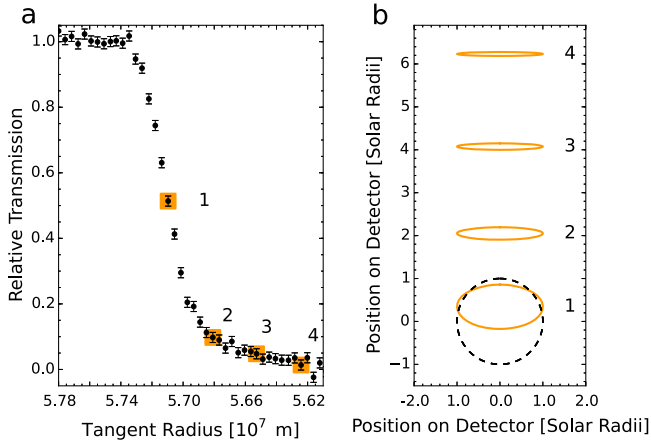
Figure 3. Two effects of atmospheric refraction captured by the occultation model. Panel a: *Cassini*-VIMS data (black data points) at 1.25 μm illustrating the decrease in transmission as the occultation progressed. Panel b: the apparent shape and position of the Sun on the VIMS detector predicted by the occultation model. The four numbered ellipses correspond to the four boxed data points in Panel a. The dashed circle is the shape and position of the unocculted Sun for reference. Since *Cassini* always pointed toward the true position of the Sun, refraction caused the apparent position of the Sun to move against the gradient in ν (radially away from the center of Saturn) as the occultation progressed. The refractive spreading of the Sun's rays flattened the appearance of the solar disk into an ellipse. Each of these effects was present in the raw VIMS data cubes, although we did not use the image of the solar disk in the raw data cubes to estimate the parameters σ_λ and ν_λ. We display these phenomena simply to demonstrate that the occultation model correctly accounted for the effects of refraction.

accounted for both the apparent motion and shrinking of the solar disk.

Having numerical functions for $\tau_\lambda(D)$ and $\alpha(D)$ meant that we could determine the relative transmission of the flux from any point on the solar disk throughout the entire occultation.[9] By integrating over the solar disk, we calculated a model value of T_λ for each r and therefore a full occultation model. Examples of the *Cassini* data and model fits in two characteristic wavelength bands are shown in Figure 4.

3.4. Bayesian Parameter Estimation

We fit the occultation model to the data and extracted the best-fit values of σ_λ, ν_λ, and H using emcee, an open source, pure-Python Markov Chain Monte Carlo ensemble sampler (Foreman-Mackey et al. 2013). In each of the 248 wavelength bands, we applied uniform priors to σ_λ and H that restricted the parameter space to 1×10^{-34} m^2 < σ_λ < 1×10^{-29} m^2 and 2.0×10^4 m < H < 8.0×10^4 m; any values of σ_λ or H outside of these ranges were considered to be unphysical based on our prior knowledge of Saturn's atmosphere. For ν_λ, we imposed a normal prior with a mean of 2.5×10^{-4} and variance of 1.6×10^{-9}. We chose these values based on known values of refractivity for H and He at a solar mixing ratio scaled to ~134 K (Atreya 1986) and based on the likely range of temperatures sampled by the occultation observations.

The posterior probability distribution function for the model parameters at 1.25 μm is shown in Figure 5. The parameter distributions for most wavelengths were well-defined and

---

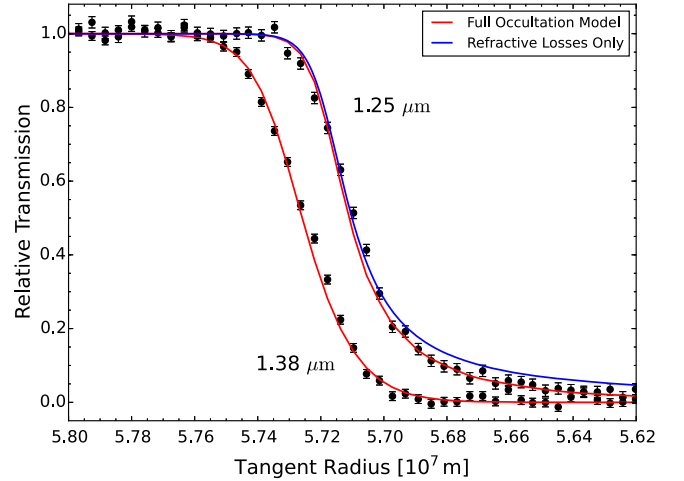**Figure 4.** *Cassini*-VIMS data (black data points) and occultation model fits at 1.25 μm—where CH$_4$ was transparent—and 1.38 μm—where CH$_4$ was opaque. Note that the tangent radius increases to the left. The dominant extinction process (refraction or absorption) and the shape of the transmission curves in these two wavelength channels were different. At 1.25 μm, the flux loss was almost entirely due to refraction, as shown by the blue curve which was found by ignoring absorption. At 1.38 μm, CH$_4$ absorption attenuated the solar flux before refractive loses became significant.
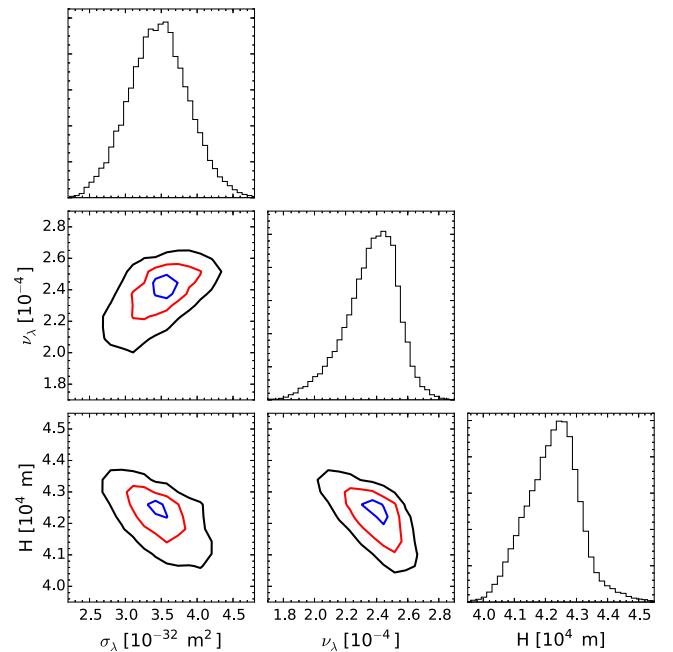

Figure 5. Posterior probability distributions for the total absorption cross section (σ_λ), the total refractivity at one bar (ν_λ), and the scale height (H) for a single wavelength band (1.25 μm). The one-dimensional histograms show the distributions for each parameter marginalized over the others and the two-dimensional histograms (with contours encompassing the 16th, 50th, and 85th percentiles) show the joint distributions for each parameter pair. The best-fit values and uncertainties found with these percentiles for σ_λ, ν_λ, and H at 1.25 μm were $3.47^{+0.42}_{-0.42} \times 10^{-32}$ m^2, $2.38^{+0.14}_{-0.18} \times 10^{-4}$, and $4.229^{+0.075}_{-0.094} \times 10^4$ m, respectively.

Gaussian. In certain cases (e.g., 1.25 μm) the distributions were skewed toward lower values of ν_λ and H. We noticed a slight correlation between these two parameters; the effect of increasing the scale height could be negated if ν_λ was allowed to reach unrealistic values greater than 1×10^{-3}. Therefore, it was necessary to impose the aforementioned prior on
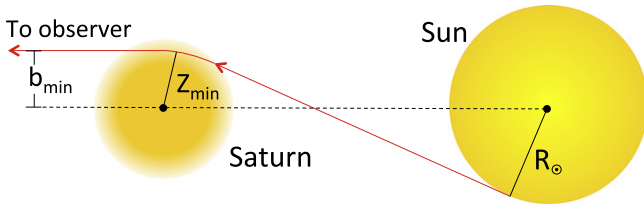
Figure 6. Geometry of a Saturn–Sun exoplanet system at mid-transit (not to scale, rings of Saturn not pictured). The path of a maximally deflected ray is shown in red. At mid-transit, in regions of the spectrum where methane was transparent, atmospheric refraction determined the minimum altitude rays could probe (z_{min}). Each z_{min} corresponded to a minimum impact parameter (b_{min}) that set the continuum level of Saturn's transmission spectrum.

refractivity. Parameter variances were higher in wavelength bands that exhibited higher noise and in two cases (1.64 and 3.88 μm) `emcee` could not produce a well-defined posterior distribution. These wavelengths corresponded to two VIMS "filter gaps" where the spectral profiles of the channels were distorted (Brown et al. 2004). We did not include these channels in our calculation of Saturn's transmission spectrum.

3.5. Transforming from Occultation to Transit

The occultation model returned parameters σ_λ and ν_λ that described the opacity and refractivity of Saturn's atmosphere between 1 and 5 μm. With these parameters, we shifted from an occultation geometry, where the observer (*Cassini*) was close to Saturn and relatively far from the Sun, to a transit geometry, where the observer was located at an infinitely large distance away from a Saturn-twin exoplanet orbiting a solar-twin star (see Figure 6). In the transit geometry, the observer only measured rays that left Saturn's atmosphere parallel to the line of sight. These rays had a range of impact parameters (b) relative to the center of the exoplanet. While in the atmosphere, the rays still refracted according to Equation (4) and experienced attenuation according to Equation (5), but the refractive spreading of the rays did not cause the apparent shrinking of the stellar disk that was present in the occultation observations.

We considered the Saturn–Sun exoplanet system at the moment of mid-transit (Figure 6). We traced rays with ~4-km vertical resolution in the upper 3% of Saturn's atmosphere[10] to determine relations between impact parameter, final optical depth (τ_λ), minimum altitude (z_{min}), and point of origin on the Sun. A ray was considered to be absorbed if it reached $\tau_\lambda \geqslant 50$. We calculated the relative transmission of each ray using $T_\lambda = e^{-\tau_\lambda}$. The 4-km vertical resolution yielded smooth numerical relations between each of the above parameters, allowing us to determine the transmission as a function of impact parameter, $T_\lambda(b)$, for Saturn at mid-transit.

We also calculated the minimum impact parameter, b_{min}, at each wavelength. In regions of the spectrum with high methane opacity, b_{min} corresponded to rays with final optical depths of ~50. This meant that absorption limited the altitudes probed by the rays. Alternatively, in regions of the spectrum where methane was transparent, atmospheric refraction determined the value of b_{min} and the rays corresponding to b_{min} had optical depths less than unity. The significance of this result will be discussed in Section 4.3.

─────────────────
[10] Rays sampling lower altitudes were absorbed.

We calculated the wavelength-dependent effective area of Saturn's disk ($A_{eff,\lambda}$) using the expression

$$A_{eff,\lambda} = \pi\left[\left(R_p + z_{top}\right)^2 - 2 \int_{b_{min}}^{R_p + z_{top}} T_\lambda(b)\, b\, db \right], \quad (6)$$

which neglects the effects of stellar limb-darkening (Bétré-mieux & Kaltenegger 2014, 2015). The integral term subtracts circular annuli of thickness db weighted by their relative transmission $T_\lambda(b)$ from the total combined area of the atmosphere and planet $\pi(R_p + z_{top})^2$. We then determined the value of transit depth δ_λ trivially using

$$\delta_\lambda = \frac{A_{eff,\lambda}}{\pi R_\odot^2}, \quad (7)$$

where $R_\odot$ is the solar radius (6.96×10^8 m). The resulting transmission spectrum of Saturn is displayed in Figure 7.

We note that our method of removing the refractive flux losses intrinsic to occultation observations, but not transit observations, differed from the methods of Robinson et al. (2014), who used *Cassini* observations to measure the transit transmission spectrum of Titan. Instead of modeling Titan's atmosphere so that $T_\lambda(b)$ could be calculated in the case of a Titan-Sun exoplanetary system, Robinson et al. (2014) divided the *Cassini* data by the correction factor

$$f_{ref} = \left(1 + d_{sc}\, d\theta/dz_{min}\right)^{-1}, \quad (8)$$

where θ is the bending angle swept out by a ray due to atmospheric refraction. This factor is simply the occultation light curve that would be produced for the case of a completely transparent atmosphere such that brightness loss is *only* due to refraction. The expression for f_{ref} was originally derived by Baum & Code (1953) under the assumption that θ was small, or, equivalently, the index of the refraction was approximately unity (Baum & Code 1953; Wasserman & Veverka 1973).

As a sanity check, we recalculated the transmission spectrum of Saturn using the methods of Robinson et al. (2014). The resulting transmission spectrum closely matched the one produced using the methods described in this work.

4. RESULTS

4.1. The Transmission Spectrum of Saturn

We generated the near-infrared transmission spectrum of Saturn as if it were a transiting exoplanet (Figure 7). The spectrum displays several spikes in transit depth of the order of 10 to 90 parts-per-million (ppm), corresponding to opacity from methane, ethane, acetylene, and possibly carbon monoxide between 4.1 and 5.0 μm. The largest feature, near 3.4 μm, is thought to be due to an asymmetric stretching mode of a C–H bond in an unknown aliphatic hydrocarbon chain. Similar chains have been identified in observations of Titan (Bellucci et al. 2009; Robinson et al. 2014) and the diffuse interstellar medium (Sandford et al. 1991). A recent analysis of Titan solar occultations by Maltagliati et al. (2015) suggested that gaseous ethane may also contribute to the opacity between 3.2 and 3.5 μm. Gaseous ethane is present in Saturn's atmosphere (Fouchet et al. 2009) and could therefore be contributing to the absorption near 3.4 μm.

The uncertainties in Saturn's transmission spectrum are the standard deviations of 1000 different transmission spectra, each
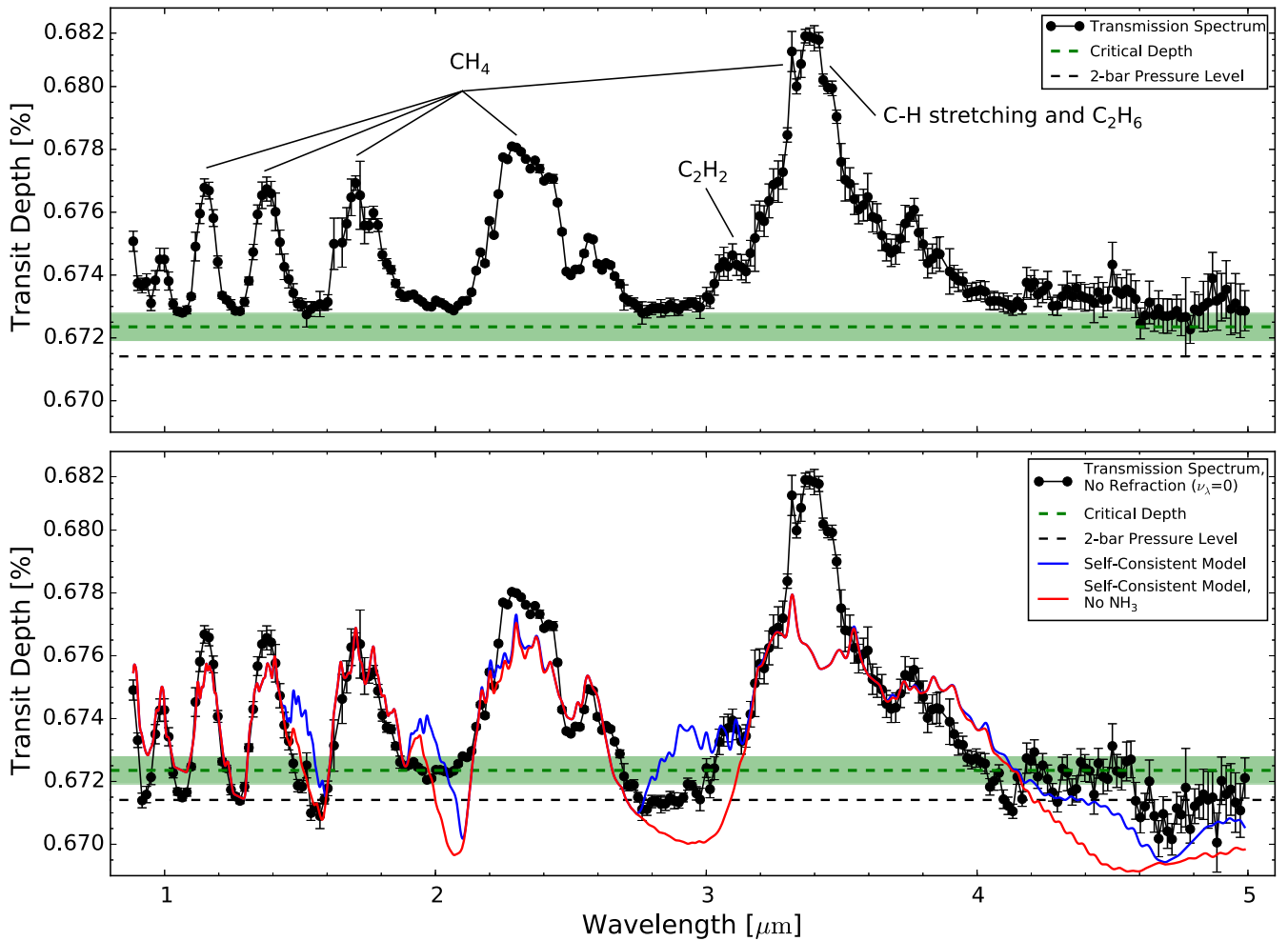
Figure 7. Top: the near-infrared, transmission spectrum of Saturn (black data points). The error bars are the 1σ uncertainties, which in some cases are smaller than the data point. The dashed green line and shaded green region correspond to the critical altitude and 1σ uncertainty range, below which rays cannot probe during mid-transit due to atmospheric refraction. The dashed black line corresponds to the two-bar pressure level in the models and presumably the top of Saturn's global NH_3 cloud layer. Bottom: Saturn's transmission spectrum generated without the effects of refraction (see Section 4.3). In this scenario, the base of the spectrum is set by a gray opacity source near the two-bar level and not the critical depth. Two self-consistent atmosphere models (blue and red) are plotted with the transmission spectrum. The blue model allows for NH_3 in gaseous form, while the red model forces the gaseous NH_3 content to zero. These models do not include the critical altitude set by refraction or the gray opacity source near two bars.

The data used to create this figure are available.

calculated using different values for parameters σ_λ, ν_λ, and H. The 1000 different parameter sets formed a Gaussian distribution that was centered on the best-fit parameters' values and with standard deviations equal to the uncertainties returned by emcee. The uncertainty was higher in the 4- to 5-μm region where the solar intensity was relatively weak.

While most of the features in the transmission spectrum were due to absorption, the baseline was determined by atmospheric refraction. This "critical transit depth" corresponded to a critical minimum altitude in Saturn's atmosphere that rays could probe during mid-transit. We found that the pressure level associated with the critical depth was 1.0 ± 0.5 bars. This value was consistent with a recent theoretical calculation of the critical pressure level for a Jupiter-sized planet with a 300-K atmosphere (Bétrémieux 2015). We note that we did not force this baseline; it is a simple geometric result of atmospheric refraction combined with the planet–star distance and the stellar radius. The baseline of the spectrum was located above a gray opacity source near two bars, which was presumably the top

NH_3 cloud deck. As a result, signatures of this feature were not detected in Saturn's transmission spectrum. The value of the critical transit depth varied slightly across the spectrum due to the uncertainty in ν_λ and the minor wavelength-dependence of refractivity in Saturn's atmosphere.

4.2. Self-consistent Atmosphere Models

Having "reconstructed" the transmission spectrum of Saturn using *Cassini*-VIMS, we next calculated the transmission spectrum of a self-consistent "off-the-shelf" atmosphere model for Saturn, following Fortney et al. (2005, 2010). The philosophy was *not* to search for a best fit, but rather to test how a model that was not tuned would fit the observations. As a transiting exoplanet, Saturn's surface gravity (10.4 m s^{-2}, Seidelmann et al. 2007) would be constrained, and the incident stellar flux around its G2V parent star at 9.524 AU (from JPL-HORIZONS, Giorgini et al. 1996) would be known. Furthermore, from the stellar age and planet mass the intrinsic flux

from the planet's interior could be assessed from evolution models (i.e., Fortney et al. 2007). With these parameters, the atmosphere code found a solution for the pressure-temperature-abundance profile that was in radiative-convective equilibrium given our knowledge of equilibrium chemistry and the wavelength-dependent opacity of each molecule. The code excluded photochemistry. Rather than solar abundances, we chose a metal-enhanced chemistry grid at $10\times$ solar, as suggested from solar system and exoplanet trends (Kreidberg et al. 2014b). The transmission spectrum of the model was calculated using the one-dimensional code described in Fortney et al. (2010).

The transmission spectrum of the self-consistent atmosphere model is shown in the bottom panel of Figure 7. Since the self-consistent models did not not include the limiting effects of refraction or the gray opacity source near two bars, it was more appropriate to compare these models to the version of Saturn's transmission spectrum that did not include refraction (see Section 4.3) than to the Saturn's actual transmission spectrum (Figure 7, top panel). To first-order, Saturn's transmission spectrum and the spectrum from the self-consistent atmosphere model showed good agreement. Yet, at various locations in the spectrum (i.e., 1.49, 1.96, and 2.93 μm), the atmosphere model exhibited opacity where the transmission spectrum of Saturn did not. These mismatches were due to the existence of gaseous ammonia at low pressures in the self-consistent model, which is not found in Saturn. The chemistry of the model naturally allowed for NH_3 condensation and depletion from the gas phase when the temperature–pressure profile became sufficiently cold. However, if the temperature–pressure profile converged to warmer temperatures at low pressures (a warm stratosphere), then the model included a reappearance of gaseous NH_3 at low pressure. In reality, Saturn's atmosphere acts like a cold trap, condensing most of the NH_3 into a cloud layer near the two-bar pressure level.

Therefore, we created a second model where all parameters were kept the same but the gaseous NH_3 abundance was forced to zero in the transmission spectrum calculation. This ammonia-free model yielded a substantially better fit to Saturn's transmission spectrum, although the following inconsistencies remained.

1. At 1.27, 1.58, 2.08, 2.96 μm, and beyond 4.20 μm the ammonia-free model decreased to values of δ_λ below the critical depth set by refraction (see Section 4.3) and even below the presumed location of the NH_3 cloud deck. In reality, rays could not probe these depths during mid-transit.

2. The self-consistent models displayed continuum absorption due to scattering by aerosols and H_2 at wavelengths shorter than 1.6 μm. Although haze is present in Saturn's atmosphere, it was not detected in the transmission spectrum.

3. The glaring disagreement near 3.4 μm resulted from gaseous ethane and an asymmetric C–H stretching mode of an unknown aliphatic hydrocarbon chain (Section 4.1).

4. Saturn's transmission spectrum displayed opacity near 3.76 μm that was not reproduced by the self-consistent atmosphere models. This feature may have been due to gaseous ethane (Sharpe et al. 2004; Maltagliati et al. 2015).

5. The peaks of the methane features at 1.15, 1.38, and 2.30 μm were underestimated by the self-consistent

atmosphere models. This may have resulted from errors in either the methane band *Cassini* data or the line-by-line opacities of methane used in the self-consistent atmosphere models (Freedman et al. 2008). Regarding the latter, recent updates to the *ExoMol* database (Yurchenko & Tennyson 2014) could potentially explain the observed discrepancies. However, the Yurchenko & Tennyson (2014) results primarily explored the opacities of methane at high temperatures, up to 1500 K. We would not expect these new line lists to be more appropriate for a model of Saturn's atmosphere (at $\sim$140 K) than the Freedman et al. (2008) results, which specifically apply to cold atmospheres. Other explanations for the discrepancies in the methane feature peaks include opacity from other unidentified species or a disequilibrium process occurring in the region sampled by the observation. Photochemical models and observations suggest that methane destruction occurs near the micro-bar level in Saturn's atmosphere (Moses et al. 2005; Fouchet et al. 2009). The production of methane deeper in Saturn's atmosphere to replenish loss due to photolysis may explain the observed excess.

4.3. Refraction and the Transmission Spectrum

Atmospheric refraction determined the minimum altitude that rays could probe during mid-transit and therefore the minimum value of transit depth in the transmission spectrum. Consequently, the transmission spectrum did not contain information about the structure or composition of the atmosphere below the critical altitude. We recalculated the transmission spectrum, forcing $\nu_\lambda = 0$ at all wavelengths in order to determine which features, if any, were blocked by refraction. In this scenario, rays traveled in straight lines through Saturn's atmosphere and the decrease in flux was entirely due to absorption (σ_λ). The resulting transmission spectrum is shown in the bottom panel of Figure 7.

The methane features in this "$\nu_\lambda = 0$" transmission spectrum were nearly identical to those in the original transmission spectrum. This was not surprising since refraction effects were minimal in those portions of the spectrum. Away from the methane features, however, rays probed deeper altitudes in Saturn's atmosphere, revealing several features that were not present in the original spectrum. First, from comparison to the one-dimensional atmosphere model we found empirical evidence for not being able to probe deeper than approximately two bars, which appeared to be due to a gray opacity source across all wavelengths, presumably the top of the NH_3 cloud layer. Second, the minimum depth near 2 μm did not appear to be set by the same feature that limited the rest of the spectrum. Instead, the opacity at 2 μm was likely due to C_2H_2 absorption.

Since rays that experienced the greatest deflection in Saturn's atmosphere originated near the solar limb, the inclusion of limb-darkening could reduce the effects of refraction on the transmission spectrum. As shown by Equation (6), including limb-darkening would result in lower T_λ-values, thereby increasing $A_{\mathrm{eff},\lambda}$. Consequently, the continuum level of the transmission spectrum may reside slightly above the critical depth set purely by atmosphere refraction. This effect would be negligible for most of Saturn's near-infrared spectrum where the variation in intensity across the

solar disk is minimal. However, limb-darkening could not be neglected at shorter wavelengths and could alter the optical transmission spectra of planets with highly refractive atmospheres. For composite transmission spectra that span multiple regimes of the electromagnetic spectrum, special care must be taken to account for stellar limb-darkening.

Calculating Saturn's transmission spectrum with $\nu_\lambda = 0$ revealed that refraction can suppress features in transmission spectra. This result has been discussed in several previous studies involving refraction and transmission spectroscopy (i.e., Sidis & Sari 2010; García Muñoz et al. 2012; Bétrémieux & Kaltenegger 2013, 2014, 2015; Misra et al. 2014). Although the effects of refraction have been largely unimportant in previous observations of hot giant exoplanet atmospheres (e.g., Hubbard et al. 2001), our results suggest that refraction may be critical to future investigations of giant, long-period exoplanet atmospheres.

5. DISCUSSION

5.1. Implications for Exoplanet Atmosphere Models

Typical models from the exoplanet atmosphere context reproduce most of the major features, due to methane absorption, across the entire wavelength range. However, the single largest absorption feature, likely due to gaseous ethane and an unknown aliphatic hydrocarbon derived from methane-based photochemistry (Atreya & Wong 2005), was absent from the model. Having opacity between 3.3 and 3.5 μm, this large feature is particularly alarming because it could influence the transit depth of an exoplanet observed in Channel 1 of the Infrared Array Camera (IRAC) on the *Spitzer Space Telescope*, which is centered at 3.6 μm (Fazio et al. 2004). This suggests that exoplanet atmospheres at all temperatures may harbor surprises that cannot be easily diagnosed with broadband photometry.

Minor disagreements between the self-consistent models and the transmission spectrum such as the peak-to-peak sizes of the methane features are also troubling. These mismatches may be caused by local disequilibrium processes (e.g., temperature variations, zonal winds) that are difficult to predict and model. As observations of exoplanet atmospheres progress to ever-greater precision, second-order effects such as these will become increasingly important.

5.2. Clouds and Transit Transmission Spectra

Although clouds are present in Saturn's atmosphere at nearly every latitude (Baines et al. 2005), Saturn's transmission spectrum is not flat to 90 ppm. Furthermore, the lowest depth a ray can probe at mid-transit is determined by refraction and not clouds.[11] Therefore, the role of clouds in the transmission spectra of cold, long-period exoplanets may not be as restrictive as that of clouds in warm Earth- and mini-Neptune-sized exoplanets. Of course, it is possible that this solar occultation only probed a relatively cloud-free portion of Saturn's atmosphere. However, variability in Saturn's cloud structure is expected to develop gradually and over large ranges of latitude and longitude (Pérez-Hoyos et al. 2006), making it unlikely that these observations were unique to a specific time or location.

---

[11] We note that the rays could likely reach the cloud deck at times before and after mid-transit (e.g., Misra et al. 2014).

5.3. Transmission Spectroscopy of Cold Gas Giants

Saturn's transmission spectrum displays molecular absorption features on the order of 90 ppm, suggesting that transmission spectroscopy is a viable technique to study the atmospheres of cold giant exoplanets. Cold atmospheres can be hosted by planets with extremely long orbital periods (such as Saturn) or by those on shorter orbits around cooler stars. Despite their rarity, giant planets orbiting later-type stars represent an accessible starting point for studies of cold giant planet atmospheres outside of the solar system. Of all the known *transiting* exoplanets, very few are expected to have cold atmospheres with methane-dominated chemistry akin to Saturn. The best candidate may be Kepler-421b, a Uranus-sized exoplanet orbiting a G9 dwarf star with a period of ∼704 days (Kipping et al. 2014). Assuming a Uranian albedo, the equilibrium temperature of Kepler-421b would be ∼185 K. Although the mass of this planet is unknown, its supposed formation location within its protostellar disk suggests that it is more likely to be an icy gas giant versus a rocky planet with a gaseous envelope (Kipping et al. 2014).

A full investigation of the detectability of molecular features in Kepler-421b's atmosphere is beyond the scope of this work. However, if the atmospheric chemistry of Kepler-421b is similar to that of Jupiter or Saturn, we might expect to see substantial methane features in the transmission spectrum. Such a detection would benefit theories of planet formation and migration and would also be the first identification of an active methane cycle occurring in an exoplanet atmosphere.

Additional giant exoplanets with cold atmospheres may be discovered in the near future. Based on expected yields from Sullivan et al. (2015), the *Transiting Exoplanet Survey Satellite* (Ricker et al. 2015) is expected to find around a half-dozen giant planets with radii of 6–22 $R_\oplus$ and periods of several hundred days. The cold atmospheres of these potential planets, in addition to that of Kepler-421b, could be probed with follow-up observations by the *Hubble Space Telescope* (*HST*) or the *James Webb Space Telescope*.

5.4. Observing a Jupiter- or Saturn-twin Exoplanet

Cold exoplanets with orbital periods of several hundred days represent a waypoint on the path toward detecting and characterizing giant planets that are analogous to those in our solar system. However, the challenges associated with observing a long-period Jupiter- or Saturn-twin exoplanet in transit necessitate a different approach than has been previously applied to short-period exoplanets. In the following sections we assess the feasibility of a survey to detect and characterize Jupiter- and Saturn-twin exoplanets in the near future.

5.4.1. Detectability and Occurrence

The a priori probability of observing a cold, long-period exoplanet in transit can be estimated by multiplying the geometric transit probability by the planet occurrence rate. For the purposes of this calculation, we consider exoplanets with periods of 4.33×10^3 days $< P < 1.08 \times 10^4$ days and masses of $0.3\,M_{\rm J} < M < 10\,M_{\rm J}$, where $M_{\rm J}$ is the mass of Jupiter and $0.3 M_{\rm J}$ is the mass of Saturn. This period range extends from that of Jupiter (∼11.9 years) to that of Saturn (∼29.5 years). We assume that all observations achieve a high enough signal-to-noise ratio to detect 100% of the

geometrically observable transits, which cause decrements in flux on the order of 1%.

The geometric transit probability for a circular orbit is the inverse of the planet's orbital distance divided by the radius of the host star: $(a/R_\star)^{-1}$. If we consider Sun-like host stars with planets in circular orbits[12] with periods in the aforementioned range, the geometric transit probability ranges from ~0.05 to ~0.09%.

Occurrence rates of Jupiter- and Saturn-like exoplanets are difficult to estimate because previous transit and radial-velocity surveys are not complete to the long periods associated with these planets. However, direct-imaging observations have suggested that the occurrences derived from radial-velocity surveys can be extrapolated to describe planets at orbital distances up to 100 AU (Brandt et al. 2014). With this in mind, we estimate the occurrence rate of Jupiter- and Saturn-like exoplanets assuming that the probability (dp) of a star hosting a planet with mass spanning $[M, M + dM]$ and orbital period spanning $[P, P + dp]$ is

$$dp = C\left(\frac{M}{M_0}\right)^{-\alpha}\left(\frac{P}{P_0}\right)^{-\beta}\frac{dM}{M}\frac{dP}{P}, \qquad (9)$$

where C, α, and β are constants and M_0 and P_0 are fiducial values chosen to be $1\,M_J$ and 1 day, respectively (Tabachnik & Tremaine 2002). We adopt the values $C = 1.04 \times 10^{-3}$, $\alpha = 0.31 \pm 0.2$, and $\beta = -0.26 \pm 0.1$ for FGK dwarf stars from Cumming et al. (2008), a radial-velocity survey completed in the ranges of 2 days $< P <$ 2000 days and $M \geqslant 0.3M_J$. As shown by Kipping et al. (2014), the Cumming et al. (2008) distribution strongly agrees with the observed occurrences rates in the *Kepler* sample (Fressin et al. 2013). We integrate Equation (9) over the ranges $[0.3M_J, 10M_J]$ and $[4.33 \times 10^3$ days, 1.08×10^4 days$]$ to find an occurrence rate of ~2.91%. Therefore, the a priori probability of observing a long-period, giant exoplanet in transit around an FGK dwarf star ranges from ~1.5 $\times$ 10^{-3} to ~2.6 $\times$ 10^{-3} percent.

Based on these probabilities, we estimate that ~38,500 stars would have to be monitored for 11.9 years in order to find a single Jupiter-analog, or ~66,700 stars for 29.5 years for a single Saturn-analog. Clearly, any survey to find long-period, giant exoplanets in transit must observe a large ($>10^5$) number of stars to make a detection on a practical timescale.

5.4.2. Survey for Long-period, Giant Exoplanets

We estimate the number of long-period (4.33×10^3 days $< P < 1.08 \times 10^4$ days), giant ($0.3M_J < M < 10M_J$) exoplanet detections around FGK dwarf stars using a stellar population generated by the Tridimensional Model of the Galaxy[13] synthesis code (TRILEGAL, Girardi et al. 2005). Using the default input parameters, we generate a stellar population in a 10 deg^2 field centered on the galactic coordinates of the *Kepler* field ($l = 76°$, $b = +14°$), with limiting H-band magnitude $m_H < 32$. Of the full sample (~3.3 $\times 10^6$ stars), we only consider stars with effective temperatures and luminosities in the fiducial ranges
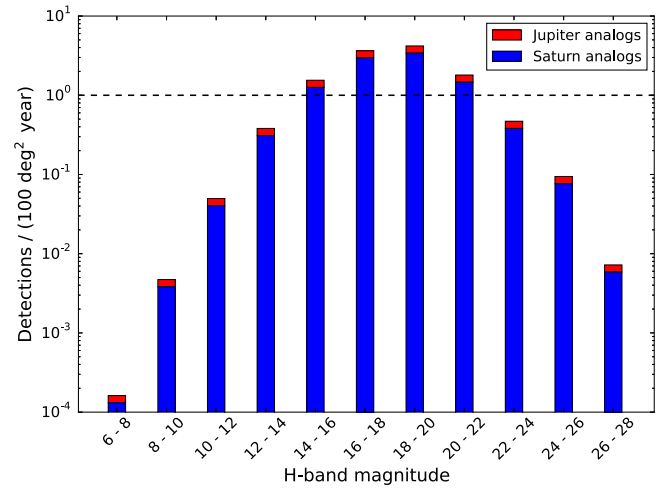
Figure 8. Expected number of long-period, giant planet transit detections per 100 deg^2 after a single year of observation. We estimate these detection rates using a synthetic catalog of FGK dwarf stars generated with the TRILEGAL simulation code (Girardi et al. 2005) and the a priori transit probabilities from Section 5.4.1. A horizontal line is drawn at unity for reference. For a Saturn-analog exoplanet, the Wide Field Camera 3 (WFC3) on board the *Hubble Space Telescope* (*HST*) could make a 5σ detection of transmission spectrum features for stars with H-band magnitudes $m_H \lesssim 9.2$. If the rates in this figure are extrapolated to cover the whole sky, we would expect one detection per year, suitable for characterization with *HST*-WFC3.

3800 K $< T_{\rm eff} <$ 7000 K and $-1.5 < \log_{10}(L/L_\odot) < 1.0$ (where $L_\odot$ is the solar luminosity) in an attempt to limit the sample to FGK dwarf stars. The stars are grouped into bins of width that are two magnitudes between $m_H = 6$ and $m_H = 28$; bins on either side of these limits contain zero stars. The total star counts in each bin are multiplied by the a priori probabilities calculated in Section 5.4.1 and divided by the periods of Jupiter and Saturn to determine the final detection rates for long-period, giant exoplanets (Figure 8). Note that we present detections per 100 deg^2 per year; TRILEGAL limits the field area to 10 deg^2, so we simply increased the number of stars in the sample by a factor of 10.

It is important to once again note that we assume that this type of survey would recover 100% of the observable transits. For reference, the transits of Jupiter and Saturn across the Sun would cause decrements in flux of ~1.1% and ~0.7%, respectively. To observe transits of this magnitude, this survey would not require a space-based telescope. Instead, arrays of ground-based, robotic telescopes, akin to MEarth (Irwin et al. 2009) or MINERVA (Swift et al. 2015), could be used to detect transit events. An all-sky, array telescope such as the "Evryscope" would also be a highly appropriate instrument for this type of survey (Law et al. 2015); the construction of the Evryscope is in part motivated by the ability to observe giant planets transiting nearby bright stars. Further characterization of these cold giant exoplanets would, however, require more powerful observing facilities.

5.4.3. Target-of-opportunity Follow-Up Observations

The long periods of these exoplanets necessitate immediate follow-up characterization. Fortunately, long periods also result in long transit durations. From the point of view of a distant observer, the transits of Jupiter and Saturn across the solar disk would last ~23 and ~57 hr, respectively.[14] These transit
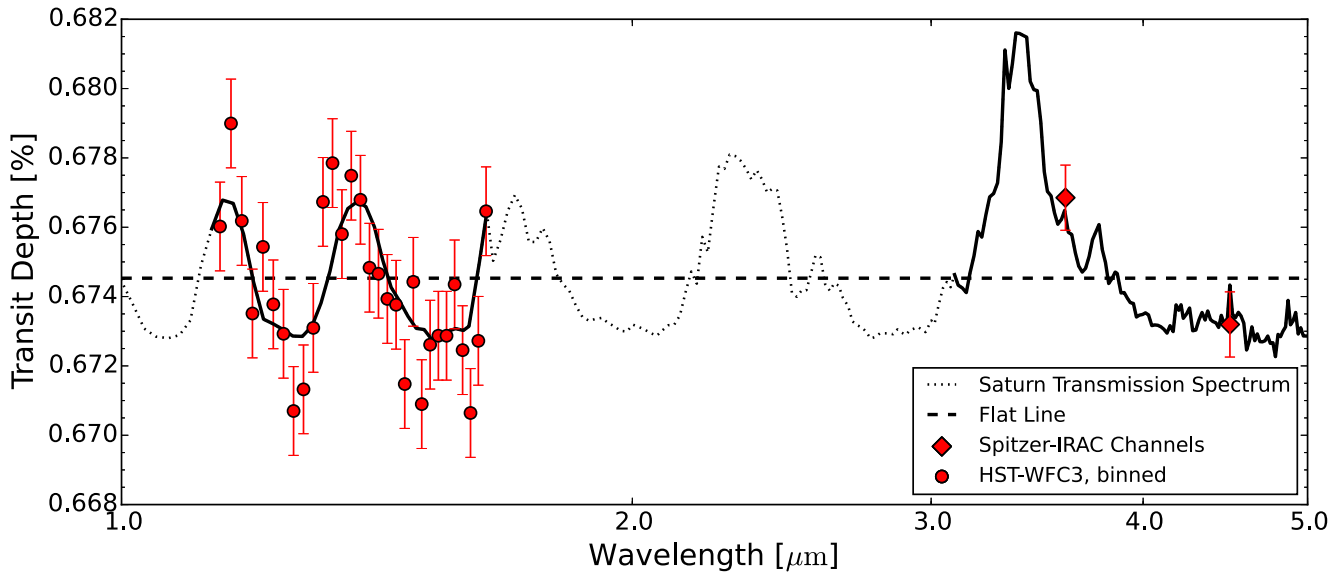
Figure 9. Simulated *HST*-WFC3 and *Spitzer*-IRAC observations of Saturn's transmission spectrum. The spectrum is solid in regions sampled by either *HST* or *Spitzer* and dotted elsewhere. The red circles are the expected *HST*-WFC3 data points, binned by 2 resolution elements and scattered with random Gaussian noise of ∼13 ppm. The red diamonds are the expected *Spitzer*-IRAC data points with an uncertainty of ∼9 ppm. Note that *Spitzer* cannot observe both channels simultaneously. In each case, the quoted precision is the requirement to distinguish the features in the transmission spectrum from a flat line (black, dashed line) to 5σ confidence. To achieve this precision in 0.5 transits of a Saturn-twin exoplanet across a solar-type star (see the text), *HST* would be limited to stars with *H*-band magnitudes $m_H \lesssim 9.2$. *Spitzer* could achieve the displayed precision in a single channel (either 3.6 or 4.5 μm) for stars with $m_H \lesssim 3.4$ but would require additional observing time to observe the the other channel. Therefore, *Spitzer* observations of this type of target are infeasible.

durations are long enough such that target-of-opportunity campaigns with facilities such as *HST* or *Spitzer Space Telescope* could be activated in time to characterize the exoplanet's atmosphere. The infrastructure for this type of observing program is already in place in the field of gamma-ray bursts (GRBs). Since 2004, the *Swift* Mission has been observing GRBs and relaying the coordinates and data to the GRB community worldwide in just a matter of seconds (Gehrels et al. 2004).

To demonstrate the ability of current facilities to characterize the atmospheres of cold giant exoplanets, we specifically consider the case of a Saturn–Sun analog observed with the Wide Field Camera 3 (WFC3) on board *HST* and the IRAC on board *Spitzer*. Upon observing the slow (∼3.3-hr), deep ingress, the survey telescopes would issue an alert calling for the activation of the target-of-opportunity programs. Under ideal conditions, *HST* could begin observing the transit 24 hr after activation,[15] capturing the final ∼29 hr of the transit. *Spitzer* normally requires 48 hr to initiate a target-of-opportunity program,[16] which leaves an insufficient amount of time to characterize the planet's atmosphere. For the purposes of this thought-experiment, however, we will consider *Spitzer*'s ability to characterize a Saturn-twin exoplanet atmosphere regardless of the 48-hr turnaround time.

In Figure 9, we show the expected *HST*-WFC3 and *Spitzer*-IRAC transmission spectrum of a Saturn-analog exoplanet derived from the *Cassini*-VIMS transmission spectrum. The spectral resolution of *HST*-WFC3 nearly matches that of *Cassini*-VIMS in this wavelength range, so a convolution to match resolution is unnecessary. We bin the high signal-to-noise ratio portion of the *HST*-WFC3 spectrum by 2 resolution elements, yielding 30 data points between 1.13 and 1.65 μm.

Then, by repeatedly scattering the data points with random Gaussian noise of 1–50 ppm, we determine that a minimum precision of 12.8 ppm is required to distinguish features in the *HST*-WFC3 spectrum from a flat line to 5σ confidence. For the simulated *Spitzer* observations, we integrate the IRAC band-passes over the transmission spectrum of Saturn to determine the 3.6 and 4.5 μm data points. We estimate that an uncertainty of 9.4 ppm is required in each *Spitzer* data point to rule out a flat spectrum to 5σ. It is critical to note that *Spitzer* cannot observe both IRAC channels simultaneously. Each data point must be obtained individually.

These uncertainties set upper limits on the magnitudes of Saturn-hosting stars that are amenable to characterization with *HST*-WFC3 and *Spitzer*-IRAC. To determine this limit for *HST*, we consider a large variety of observing strategies (e.g., staring versus spatial scan modes, various slew rates (McCullough & MacKenty 2012), subarray sizes, and readout configurations) over a range of *H*-band magnitudes matching the output from the TRILEGAL simulation ($6 < m_H < 28$). In each case, we assume that *HST* observes the transiting system for 36 consecutive orbits: 18 during the final half of transit, and 18 out-of-transit orbits to establish a precise baseline for the stellar flux. We assume that the host star is visible for 56 minutes of the 96-minute orbit before Earth occultation, similar to the stars in the *Kepler* field. The nominal exposure time is set by the chosen readout configuration, and the corresponding signal-to-noise ratio per resolution element per exposure is estimated using the *HST*-WFC3 exposure time calculator.[17] For each observing configuration, we use the Phase II Astronomer's Proposal Tool[18] Orbit Planner to determine the number of exposures we can obtain per *HST* orbit and make a final estimate of the precision of the transmission spectrum.

---

[15] http://www.stsci.edu/hst/HST_overview/documents/uir/ToO-UIR.pdf
[16] http://ssc.spitzer.caltech.edu/warmmission/ddttoo/whattoo/
[17] http://etc.stsci.edu/etc/input/wfc3ir/spectroscopic/
[18] http://www.stsci.edu/hst/proposing/apt/

The result of this calculation is that with only a half transit, *HST*-WFC3 can make a 5σ detection of atmospheric features in the transmission spectrum of a Saturn-analog if the host star has $m_H \lesssim 9.2$. As displayed in Figure 8, fewer than one Saturn-analog detection is expected per 100 deg^2 per year. However, if we extrapolate these detection rates to cover the entire sky, we would expect approximately one detection per year, amenable to characterization with *HST*-WFC3.

Considering that *Spitzer* cannot respond quickly enough to characterize a transiting Saturn-analog exoplanet and that each channel must be observed individually, we estimate its limiting host-star magnitude in less detail than for *HST*. If we assume photon-limited observations, we can loosely estimate uncertainties by scaling those obtained for a previous *Spitzer*-IRAC observation of a solar-type star. For 55 Cancri ($m_H = 4.14$), Demory et al. (2011) achieved 63-ppm-precision in IRAC's 4.5 μm band over 4.97 hr of observation. If *Spitzer*-IRAC could only observe 0.5 transits (29 hr in transit +29 hr out of transit) of a Saturn-twin exoplanet orbiting a solar-type star *in a single channel*, then the 9.4 ppm precision requirement would limit the host star H-band magnitudes to $m_H \lesssim 3.4$. *Spitzer* would then have to wait until the following transit event to obtain observations in the other channel. This first-order approximation demonstrates that *HST* is by far the most appropriate currently operational instrument for characterizing the atmospheres of cold, long-period exoplanets.

The success of this hypothetical survey is contingent upon the ability of the survey telescopes to quickly and accurately identify long-period, giant exoplanet transits. This would require immediate, automatic data reduction and analysis. For stars brighter than $m_H \approx 9.2$ and transit durations longer than $\sim$57 hr, there is some flexibility that would allow for human intervention. Still, distinguishing false positives from actual events would be a major challenge to this approach. As in any other wide-field transit survey, false alarms may result from variations in instrument sensitivity, weather, or other astrophysical sources such as stellar variability or unknown stellar companions. To the extent that it is possible, explicit target selection and advance "snapshot" observations could limit astrophysical false positives. To reduce the false positives due to eclipsing binary stars, the target-of-opportunity program could also involve obtaining a spectrum of the target in search of two sets of spectral lines.

6. CONCLUDING REMARKS

Studies of solar system analogs provide a useful method of "ground-truthing" the techniques and models frequently applied to exoplanets. Exhausting the resources provided by decades of work in the planetary sciences will greatly aid the burgeoning field of exoplanetary science. The usefulness of missions such as *Cassini* and Juno, which is currently *en route* to Jupiter, extends beyond the solar system to the cold, long-period regime of exoplanets.

The *Kepler* Mission has discovered a great variety of Earth-sized exoplanets. Future efforts to discover and characterize cold Jupiters and Saturns may find that a similar diversity exists among giant gaseous planets. These efforts will put the giant members of our solar system in a greater context, thereby allowing for a better understanding of the formation and evolution of our entire solar system.

REFERENCES

Atreya, S. K. 1986, Atmospheres and Ionospheres of the Outer Planets and their Satellites (Berlin: Springer)
Atreya, S. K., & Wong, A.-S. 2005, SSRv, 116, 121
Bagenal, F., Dowling, T. E., & McKinnon, W. B. 2004, Jupiter: The Planet, Satellites and Magnetosphere (Cambridge: Cambridge Univ. Press)
Baines, K. H., Drossart, P., Momary, T. W., et al. 2005, EM&P, 96, 119
Baum, W. A., & Code, A. D. 1953, AJ, 58, 108
Bean, J. L., Miller-Ricci Kempton, E., & Homeier, D. 2010, Natur, 468, 669
Beatty, T. G., & Gaudi, B. S. 2008, ApJ, 686, 1302
Bellucci, A., Sicardy, B., Drossart, P., et al. 2009, Icar, 201, 198
Berta, Z. K., Charbonneau, D., Désert, J.-M., et al. 2012, ApJ, 747, 35
Bétrémieux, Y. 2015, MNRAS, submitted (arXiv:1509:03984)
Bétrémieux, Y., & Kaltenegger, L. 2013, ApJL, 772, L31
Bétrémieux, Y., & Kaltenegger, L. 2014, ApJ, 791, 7
Bétrémieux, Y., & Kaltenegger, L. 2015, MNRAS, 451, 1268
Birkby, J. L., de Kok, R. J., Brogi, M., et al. 2013, MNRAS, 436, L35
Brandt, T. D., McElwain, M. W., Turner, E. L., et al. 2014, ApJ, 794, 159
Brogi, M., de Kok, R. J., Birkby, J. L., Schwarz, H., & Snellen, I. A. G. 2014, A&A, 565, A124
Brown, R. H., Baines, K. H., Bellucci, G., et al. 2004, SSRv, 115, 111
Cabrera, J., Csizmadia, S., Lehmann, H., et al. 2014, ApJ, 781, 18
Carson, J., Thalmann, C., Janson, M., et al. 2013, ApJL, 763, L32
Charbonneau, D., Brown, T. M., Noyes, R. W., & Gilliland, R. L. 2002, ApJ, 568, 377
Cox, A. N. 2000, Allen's Astrophysical Quantities (Berlin: Springer)
Cumming, A., Butler, R. P., Marcy, G. W., et al. 2008, PASP, 120, 531
Demory, B.-O., Gillon, M., Deming, D., et al. 2011, A&A, 533, A114
Ehrenreich, D., Bonfils, X., Lovis, C., et al. 2014, A&A, 570, A89
Fazio, G. G., Hora, J. L., Allen, L. E., et al. 2004, ApJS, 154, 10
Foreman-Mackey, D., Hogg, D. W., Lang, D., & Goodman, J. 2013, PASP, 125, 306
Fortney, J. J., Marley, M. S., & Barnes, J. W. 2007, ApJ, 659, 1661
Fortney, J. J., Marley, M. S., Lodders, K., Saumon, D., & Freedman, R. 2005, ApJL, 627, L69
Fortney, J. J., Shabram, M., Showman, A. P., et al. 2010, ApJ, 709, 1396
Fouchet, T., Moses, J. I., & Conrath, B. J. 2009, Saturn from Cassini-Huygens Chemistry, ed. M. K. Dougherty, L. W. Esposito & S. M. Krimigis (Berlin: Springer), 83
Fraine, J., Deming, D., Benneke, B., et al. 2014, Natur, 513, 526
Freedman, R. S., Marley, M. S., & Lodders, K. 2008, ApJS, 174, 504
Fressin, F., Torres, G., Charbonneau, D., et al. 2013, ApJ, 766, 81
García Muñoz, A., Zapatero Osorio, M. R., Barrena, R., et al. 2012, ApJ, 755, 103
Gehrels, N., Chincarini, G., Giommi, P., et al. 2004, ApJ, 611, 1005
Giorgini, J. D., Yeomans, D. K., Chamberlin, A. B., et al. 1996, BAAS, 28, 1158
Girardi, L., Groenewegen, M. A. T., Hatziminaoglou, E., & da Costa, L. 2005, A&A, 436, 895
Han, E., Wang, S. X., Wright, J. T., et al. 2014, PASP, 126, 827
Hubbard, W. B., Dougherty, M. K., Gautier, D., & Jacobson, R. 2009, Saturn from Cassini-Huygens Interior of Saturn, ed. M. K. Dougherty, L. W. Esposito & S. M. Krimigis (Berlin: Springer), 75
Hubbard, W. B., Fortney, J. J., Lunine, J. I., et al. 2001, ApJ, 560, 413

Ida, S., & Lin, D. N. C. 2004, ApJ, 604, 388
Irwin, J., Charbonneau, D., Nutzman, P., & Falco, E. 2009, in IAU Symp. 253, ed. F. Pont, D. Sasselov & M. J. Holman (Cambridge: Cambridge Univ. Press), 37
Irwin, P. G. J., Barstow, J. K., Bowles, N. E., et al. 2014, Icar, 242, 172
Irwin, P. G. J., Teanby, N. A., de Kok, R., et al. 2008, JQSRT, 109, 1136
Jenkins, J. M., Twicken, J. D., Batalha, N. M., et al. 2015, AJ, 150, 56
Kane, S. R. 2011, Icar, 214, 327
Kipping, D. M. 2013, MNRAS, 434, L51
Kipping, D. M. 2014, MNRAS, 444, 2263
Kipping, D. M., Torres, G., Buchhave, L. A., et al. 2014, ApJ, 795, 25
Kivalov, S. N. 2007, ApOpt, 46, 7091
Knutson, H. A., Benneke, B., Deming, D., & Homeier, D. 2014a, Natur, 505, 66
Knutson, H. A., Charbonneau, D., Noyes, R. W., Brown, T. M., & Gilliland, R. L. 2007, ApJ, 655, 564
Knutson, H. A., Dragomir, D., Kreidberg, L., et al. 2014b, ApJ, 794, 155
Kreidberg, L., Bean, J. L., Désert, J.-M., et al. 2014a, Natur, 505, 69
Kreidberg, L., Bean, J. L., Désert, J.-M., et al. 2014b, ApJL, 793, L27
Lagrange, A.-M., Bonnefoy, M., Chauvin, G., et al. 2010, Sci, 329, 57
Law, N. M., Fors, O., Ratzloff, J., et al. 2015, PASP, 127, 234
Lindal, G. F., Lyons, J. R., Sweetnam, D. N., Eshleman, V. R., & Hinson, D. P. 1987, JGR, 92, 14987
Line, M. R., Knutson, H., Wolf, A. S., & Yung, Y. 2014, ApJ, 783, 70
Line, M. R., & Yung, Y. L. 2013, ApJ, 779, 3
Madhusudhan, N., Amin, M. A., & Kennedy, G. M. 2014, ApJL, 794, L12
Madhusudhan, N., & Seager, S. 2009, ApJ, 707, 24
Maltagliati, L., Bézard, B., Vinatier, S., et al. 2015, Icar, 248, 1
Marois, C., Macintosh, B., Barman, T., et al. 2008, Sci, 322, 1348
Matson, D. L., Spilker, L. J., & Lebreton, J.-P. 2002, SSRv, 104, 1
McCord, T. B., Coradini, A., Hibbitts, C. A., et al. 2004, Icar, 172, 104
McCullough, P., & MacKenty, J. 2012, Considerations for Using Spatial Scans with WFC3 Tech. Rep. (Baltimore, MD: STScI), 2012-08
Misra, A., Meadows, V., & Crisp, D. 2014, ApJ, 792, 61
Montañés-Rodríguez, P., González-Merino, B., Pallé, E., López-Puertas, M., & García-Melendo, E. 2015, ApJL, 801, L8
Moses, J. I., Fouchet, T., Bézard, B., et al. 2005, JGRE, 110, 8001
Öberg, K. I., Murray-Clay, R., & Bergin, E. A. 2011, ApJL, 743, L16

Orosz, J. A., Welsh, W. F., Carter, J. A., et al. 2012, Sci, 337, 1511
Owen, T., Mahaffy, P., Niemann, H. B., et al. 1999, Natur, 402, 269
Pallé, E., Zapatero Osorio, M. R., Barrena, R., Montañés-Rodríguez, P., & Martín, E. L. 2009, Natur, 459, 814
Pérez-Hoyos, S., Sánchez-Lavega, A., & French, R. G. 2006, A&A, 460, 641
Pollack, J. B., Hubickyj, O., Bodenheimer, P., et al. 1996, Icar, 124, 62
Pont, F., Knutson, H., Gilliland, R. L., Moutou, C., & Charbonneau, D. 2008, MNRAS, 385, 109
Ricker, G. R., Winn, J. N., Vanderspek, R., et al. 2015, JATIS, 1, 014003
Robinson, T. D., Maltagliati, L., Marley, M. S., & Fortney, J. J. 2014, PNAS, 111, 9042
Sandford, S. A., Allamandola, L. J., Tielens, A. G. G. M., et al. 1991, ApJ, 371, 607
Schwieterman, E. W., Robinson, T. D., Meadows, V. S., Misra, A., & Domagal-Goldman, S. 2015, ApJ, 810, 57
Seidelmann, P. K., Archinal, B. A., A'Hearn, M. F., et al. 2007, CeMDA, 98, 155
Sharpe, S. W., Johnson, T. J., Sams, R. L., et al. 2004, ApSpe, 58, 1452
Sidis, O., & Sari, R. 2010, ApJ, 720, 904
Smith, B. A., Soderblom, L. A., Banfield, D., et al. 1989, Sci, 246, 1422
Smith, G. R., Shemansky, D. E., Holberg, J. B., et al. 1983, JGR, 88, 8667
Snellen, I. A. G., de Kok, R. J., de Mooij, E. J. W., & Albrecht, S. 2010, Natur, 465, 1049
Stevenson, K. B., Bean, J. L., Madhusudhan, N., & Harrington, J. 2014, ApJ, 791, 36
Sullivan, P. W., Winn, J. N., Berta-Thompson, Z. K., et al. 2015, ApJ, 809, 77
Swift, J., Botton, M., Johnson, J. A., et al. 2015, JATIS, 1, 027002
Tabachnik, S., & Tremaine, S. 2002, MNRAS, 335, 151
Tokunaga, A. T., Orton, G. S., & Caldwell, J. 1983, Icar, 53, 141
van der Werf, S. Y. 2008, ApOpt, 47, 153
Vidal-Madjar, A., Arnold, L., Ehrenreich, D., et al. 2010, A&A, 523, A57
Wasserman, L. H., & Veverka, J. 1973, Icar, 20, 322
Welsh, W. F., Orosz, J. A., Carter, J. A., et al. 2012, Natur, 481, 475
West, R. A., Baines, K. H., Karkoschka, E., & Sánchez-Lavega, A. 2009, Clouds and Aerosols in Saturn's Atmosphere, ed. M. K. Dougherty, L. W. Esposito & S. M. Krimigis, 161
Yurchenko, S. N., & Tennyson, J. 2014, MNRAS, 440, 1649